

Article

N,S Co-Doped Carbon Nanofibers Derived from Bacterial Cellulose/Poly(Methylene Blue) Hybrids: Efficient Electrocatalyst for Oxygen Reduction Reaction

Jing Liu ¹, Yi-Gang Ji ², Bin Qiao ¹, Fengqi Zhao ³, Hongxu Gao ³, Pei Chen ^{1,*}, Zhongwei An ¹, Xinbing Chen ¹ and Yu Chen ¹

¹ Key Laboratory of Applied Surface and Colloid Chemistry (MOE); Shaanxi Key Laboratory for Advanced Energy Devices; Shaanxi Engineering Lab for Advanced Energy Technology, School of Materials Science and Engineering, Shaanxi Normal University, Xi'an 710119, China; liujing551177@gmail.com (J.L.); qiaobin0229@gmail.com (B.Q.); gmecazw@163.com (Z.A.); chenxinbing@snnu.edu.cn (X.C.); ndchenyu@gmail.com (Y.C.)

² Jiangsu Key Laboratory of Biofunction Molecule, Department of Life Sciences and Chemistry, Jiangsu Second Normal University, Nanjing 210013, China; ygji@jssnu.edu.cn

³ National Key Laboratory of Science and Technology on Combustion and Explosion, Xi'an Modern Chemistry Research Institute, 168 East Zhangba Road, Xi'an 710065, China; zhaofqi@163.com (F.Z.); gordon888@163.com (H.G.)

* Correspondence: chenpei@snnu.edu.cn; Tel.: +86-029-8153-0719

Received: 26 May 2018; Accepted: 27 June 2018; Published: 30 June 2018



Abstract: Exploring inexpensive and highly efficient electrocatalyst to decrease the overpotential of oxygen reduction reaction (ORR) is one of the key issues for the commercialization of energy conversion and storage devices. Heteroatom-doped carbon materials have attracted increasing attention as promising electrocatalysts. Herein, we prepared a highly active electrocatalyst, nitrogen, sulfur co-doped carbon nanofibers (N/S-CNF), via in situ chemical oxidative polymerization of methylene blue on the bacterial cellulose nanofibers, followed by carbonization process. It was found that the type of nitrogen/sulfur source, methylene blue and poly(methylene blue), has significantly influence on the catalytic activity of the resultant carbon nanofibers. Benefiting from the porous structure and high surface area (729 m²/g) which favors mass transfer and exposing of active N and S atoms, the N/S-CNF displays high catalytic activity for the ORR in alkaline media with a half-wave potential of about 0.80 V, and better stability and stronger methanol tolerance than that of 20 wt % Pt/C, indicating great potential application in the field of alkaline fuel cell.

Keywords: nitrogen sulfur co-doped carbon nanofibers; bacterial cellulose/poly(methylene blue) hybrids; oxygen reduction reaction; electrocatalyst

1. Introduction

The development of low-cost and efficient energy conversion and storage technologies is of vital importance in alleviating the energy crisis and environmental protection. In recent years, some novel fuel cells and metal-air batteries, a class of devices that convert the chemical energy directly into electricity by electrochemical reactions, have attracted increasing attention [1–4]. In these devices, the oxygen reduction reaction (ORR) on the cathode is very slow kinetically, and thus requires platinum (Pt) as electrocatalyst. As the high price and unsatisfactory methanol tolerance of Pt have become a bottleneck of its extensive application in the fuel cells and metal-air batteries, the development of cheap and steady non-platinum catalysts is a practical and urgent issue [5–8]. In such conditions,

nitrogen doped carbon nanomaterials (N-Cs) has recently been expanding rapidly because of excellent catalytic activity and high stability for the ORR in alkali media, and many techniques have been developed to prepare high active N-Cs as electrocatalyst for the ORR [9–14].

It is very well-known that the catalytic activity of N-Cs is closely related to their structure, meanwhile, the structural characteristics, such as the type and number of active centers, the porous structures [15] and the graphitizing extent [16,17], are controlled by the preparation method. Generally, the most used method to prepare the N-Cs is carbonizing various nitrogen-containing precursors, including (i) the heat-treatment of the existing carbon materials (such as graphene) using N-containing compounds (ammonia etc.); (ii) the pyrolysis of the N,C-containing precursor. In these processes, nitrogen source has great influence on the structure characteristics of the resultant N-Cs, and thus has a positive or negative impact on the catalytic activity for the ORR [18,19]. Understanding the impact of nitrogen source in molecular scale will provide fundamental knowledge for the rational design of N-Cs with high catalytic activity for the ORR.

In addition to the nitrogen source, the carbon source should be paid much attention to. Most of the reported N-Cs are prepared through chemical reagents or pre-synthesized precursor [20,21]. Considering the mass production in practical application, the cheaper raw and more convenient procedures are desired. Biomass is an attractive raw material due to its low cost, abundance and environmental friendly. Recently, various biomass, such as soybean shells [22], poplar catkins [23], biomass lysine [24] and soybean [25], are used to prepare the N-Cs as electrocatalyst for the ORR. Compare to these materials, cellulose, as the most abundant polymer on earth, is an excellent precursor for producing various carbon-based catalyst [23,26]. Especially, bacterial cellulose (BC), a biomass material produced by microbial industrial fermentation process at a very low price, possess a interconnected three dimension porous network structure consisting of cellulose nanofibers, and thus, is an ideal material to prepare of three dimension carbon-based functional nanomaterials [27,28].

Methylene blue (MB), as a cationic phenothiazines dye, contains not only N but also S element. Both can incorporate into the carbon matrix through facile carbonization, and the synergistic effect of N and S further enhances the catalysis performance for the ORR [29]. In addition, MB has good adsorption on the phenolic group of BC through various mechanisms such as electrostatic attractions [30], and it is easy to obtain the hybrid of BC/MB. Though carbonizing it, the nitrogen, sulfur-co-doped carbon nanofibers (N/S-CNF) has been facily achieved [31]. However, compared with the comical Pt/C, the catalytic activity of N/S-CNF for the ORR is unsatisfied, and there is still no rational explanation for this result, due to the complicated carbonation process [32].

Compared with MB which is a small molecule compound, poly(methylene blue) (PMB) can gradually reduce and release the N/S-containing gas products during the carbonization process. These gas products readily react with the carbonization product and incorporate into it with higher N/S doping amount. Hence, we speculate that poly(methylene blue) (PMB) may be more appropriate as nitrogen source than MB. Luckily, the chemical oxidative polymerization of MB can occur at room temperature using the common oxidant, such as Au^{3+} and ammonium persulfate ($(\text{NH}_4)_2\text{S}_2\text{O}_8$) [33,34].

Therefore, in this work, using BC as carbon source, MB and PMB as nitrogen source respectively, the N/S-CNF was prepared. After characterizing the microstructure and evaluating the catalytic activity of the N/S-CNF derived from the hybrids of BC/MB and BC/PMB respectively, it is found that the activity for the ORR can be tuned by varying the type of nitrogen precursor. The N/S-CNF, prepared via in situ chemical oxidative polymerization of MB on the BC followed by carbonization process, displays high catalytic activity for the ORR in alkaline media with a half-wave potential of about 0.80 V, and better stability and stronger methanol tolerance than that of 20 wt % Pt/C.

2. Results

2.1. Characterization of the BC/MB and BC/PMB

As presented in Figure 1, the N/S-CNF were prepared by three steps. First, the MB was adsorbed on the surface of BC at 100 °C, driven by the electrostatic interaction or hydrogen bond. Secondly, the chemical oxidative polymerization of MB was initiated by $(\text{NH}_4)_2\text{S}_2\text{O}_8$ and the formed PMB wrapped evenly the nanofibers of BC [34]. Finally, the obtained BC/PMB hybrid was carbonized to form the N/S-CNF.

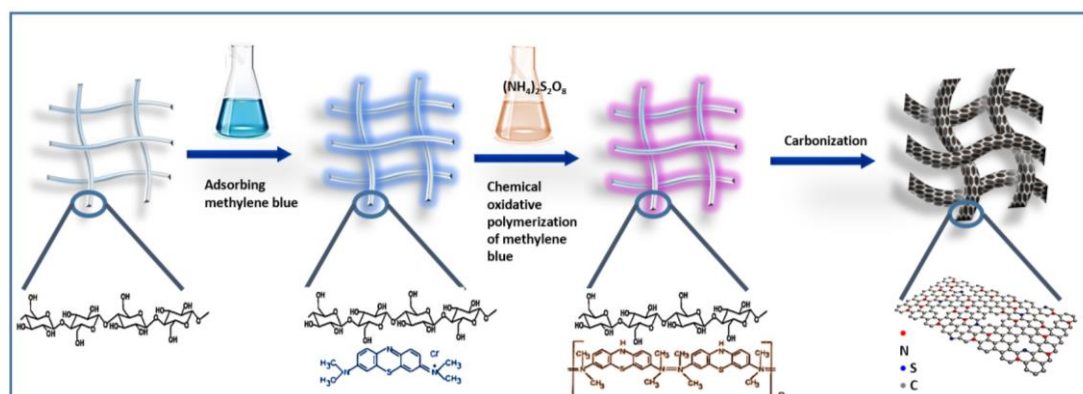


Figure 1. Synthetic procedure of the N/S-CNF.

To identify the formation of PMB on the surface of BC, the samples of BC, BC/MB and BC/PMB were characterized. Scan electron microscopy (SEM) image (Figure 2a) shows that the BC consists of the intertwining nanofibers with a dimension of about 100 nm. After adsorbing MB, some MB particle aggregations are deposited on the surface of BC (Figure 2b). However, after polymerization, these aggregations disappear and some smooth joints gumming the nanofiber together are observed from the BC/PMB (Figure 2c), suggesting the dissolution/reprecipitation process happened during the chemical oxidation polymerization of MB. The EDS results show that N, S and Cl are detected in the BC/MB and BC/PMB, and the contents of N and S in these two samples are similar (Figure 2b,c and Figure S1). However, the content of Cl in the BC/PMB is much lower than that of the BC/MB. This result indicates that, the MB cations are adsorbed on the surface of BC by static electric attractive, after in situ oxidation polymerization, Cl^- dissolved into solution and the electroneutral PMB was formed. From the FTIR spectra of BC, PMB, and BC/PMB in Figure 2d, the typical peaks belonging to the PMB and BC, which are in agreement with the reported [35–38], are observed. The peak at 1600 cm^{-1} assigned to the stretching vibration of the $-\text{C}=\text{N}$ group of the PMB is detected from the BC/PMB, demonstrating that the PMB has successfully loaded on the BC. In addition, the survey spectra of X-ray photoelectron spectroscopy (XPS) (Figure 2e) further prove the presence of S and N in both the BC/MB and BC/PMB. Similar to the results of EDS, the peak (198.9 eV) ascribed to Cl^- is detected from the BC/MB while not the BC/PMB. The XPS fine spectra of N1s in Figure 2f further demonstrates the formation of PMB in the BC/PMB due to the appearance of PMB characteristic peak at 400.1 eV [39]. Furthermore, the peaks of pyridinic N (399.7 eV) and protonated amine N (401.6 eV) of the PMB shift to low energy direction, indicating the PMB tightly wraps the nanofibers of BC, which results in the electron of the skeleton carbon atoms in the BC shifting toward the N atom of PMB due to the difference in electronegativity between them. All these results reveal that the hybrid of BC/PMB has been successfully prepared. Further study (Figure S2) reveals that, without the BC, the prepared PMB are blocks with irregular morphology, testifying the important role of BC in inhibiting the agglomeration of PMB.

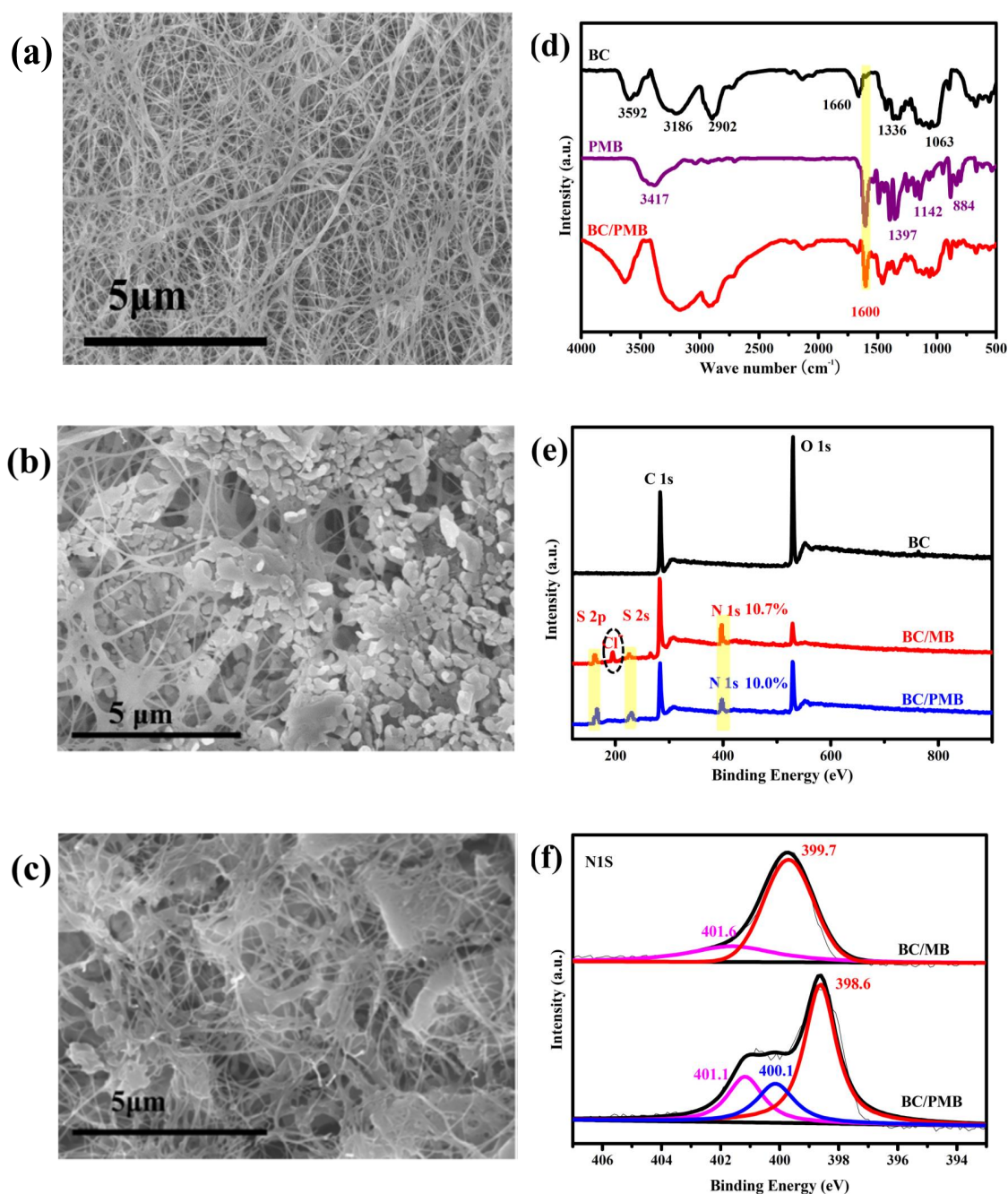


Figure 2. SEM images of (a) BC; (b) BC/MB and (c) BC/PMB; (d) FTIR spectra of BC, PMB and BC/PMB; (e) XPS survey spectra of BC, BC/MB and BC/PMB; and (f) fine XPS spectra of N1s for the BC/MB and BC/PMB.

Thermogravimetric analysis (TGA) was further carried out to verify the thermal decomposition behavior of the BC, MB, PMB, BC/MB and BC/PMB, and the corresponding TG curves are shown in Figure 3. The MB exhibits the first mass loss step below 250 °C with a mass loss of about 13%, and the second one centers at 250–400 °C with a mass loss of about 26%. With further increasing the temperature, the mass loss increases slowly, and the carbon product at 800 °C is about 52%. Compared with the MB, PMB shows much better thermal stability, and the onset decomposition temperature is up to ~250 °C, but the carbon yield has no change. The BC has a sharp mass loss in the range of 250–375 °C, and a low carbon yield of 11%. For the BC/MB, the thermal decomposition

behavior in the low temperature (<250 °C) is similar to that of MB, and the carbon yield is ~40%. No surprise, the BC/PMB displays higher thermal stability below 250 °C, and the carbon yield is close to that of BC/MB and of 37%. Based on these results, it can be suspected that the high decomposition temperature of PMB should be helpful for its decomposition products to participate in the carbonization reaction, and thus promote the formation of N/S co-doped carbon materials.

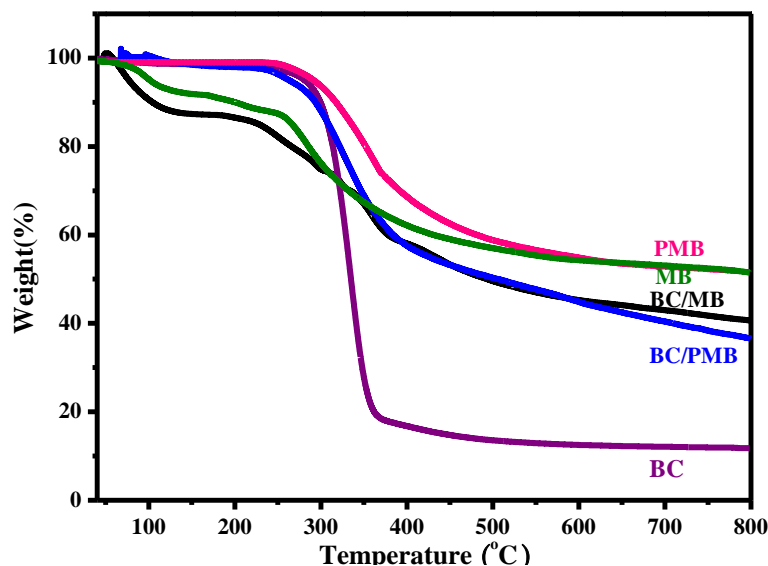


Figure 3. TG curves of the PMB, MB, BC, BC/MB and BC/PMB.

2.2. Characterization of the Carbonization Products of BC, BC/MB and BC/PMB

After carbonizing the BC, BC/MB and BC/PMB, the resultant products are named by C-BC, C-BC/MB and N/S-CNF, and their morphologies were investigated by SEM and TFM. Compared the images of BC (Figure 2a) and C-BC (Figure 4a,c), no obvious change is observed, except that the nanofibers are fluffier and thinner in the case of C-BC. However, compared with the BC/MB (Figure 2b), the C-BC/MB (Figure 4b) exhibits quite different morphology, which is similar to that of C-BC, seeming that MB particles have been completely decomposed. Nevertheless, the corresponding transmission electron microscopy (TEM) image (Figure 4e) shows that, except for the nanofibers derived from the BC, there are some isolated nanoparticles with a dimension of about 30 nm. Based on the different Z-contrast between S and C elements, these nanoparticles should be the sulfur-rich materials, which are proved by the element mapping results of energy dispersive spectrometer (EDS) (Figure S3). Obviously, these nanoparticles are the carbonized products coming from the incomplete decomposition of MB, due to the absence of S in the BC. Considering the similar morphology of the carbon nanofibers in cases of C-BC and C-BC/MB, it is deduced that the adsorbed MB has little influence on the decomposition of BC, probably due to the weak interface interaction between them, just as shown the TG curve in Figure 3. It is interesting to note that, in contrast to the C-BC and C-BC/MB, the N/S-CNF derived from the BC/PMB, consists of some short and wide nanobelts (Figure 4c), and their diameter and length (Figure S4) are about 70 and 400 nm, respectively. This result demonstrates the great influence of PMB on the carbonization of BC. TEM image in Figure 4e shows that the contrast of the nanobelts is uniform, indicating the absence of sulfur-rich domains in the N/S-CNF. In addition, elemental mappings from energy dispersive spectroscopy (EDS) (Figure 4h,i) confirm the nitrogen and sulfur are successfully incorporated and uniformly distribute in the carbon matrix. Moreover, EDS results (insets in Figure 4b,c) show that the contents of N and S are slightly higher in the case of N/S-CNF than that of C-BC/MB, further proving that PMB as N/S source is helpful for the incorporation of N/S into the carbon framework. No Cl was found by EDS, probably because of the formation of Cl-containing gas.

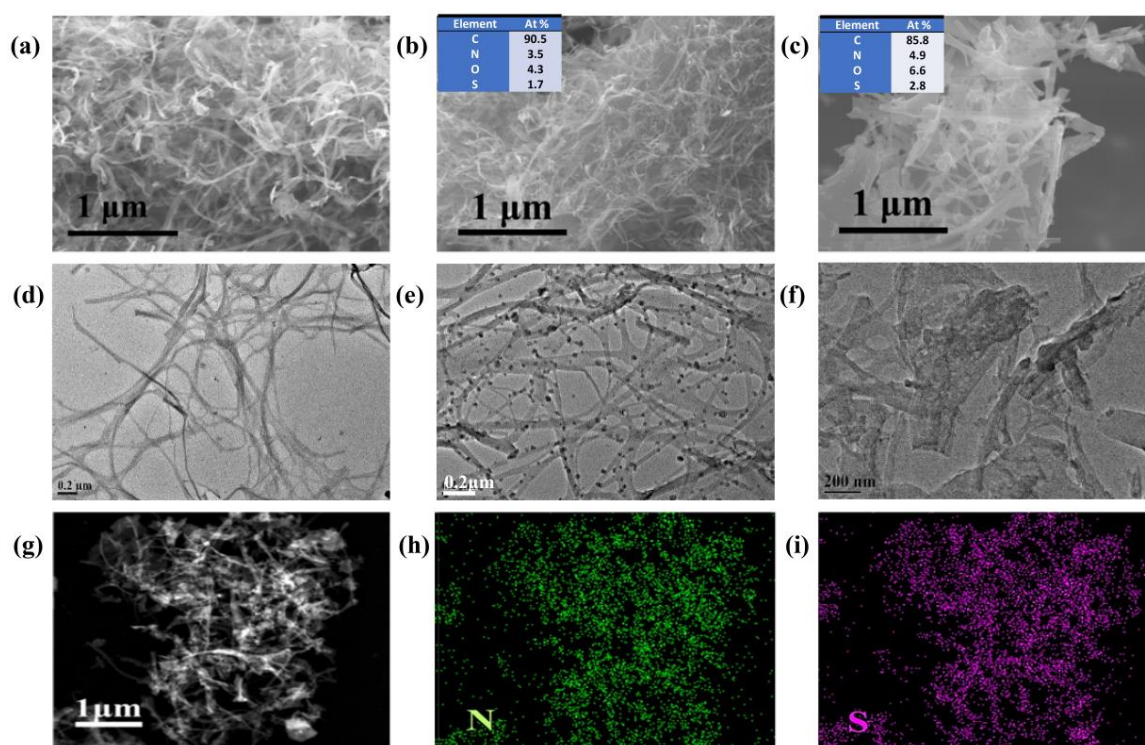


Figure 4. SEM and TEM images of the (a,d) C-BC; (b,e) C-BC/MB and (c,f) N/S-CNF; and the element maps (g–i) of N,S-CNF. The insets in (b,c) are EDS data.

To gain more insight, the porous structure of N/S-CNF was characterized. As shown in Figure 5a, with respect to the C-BC and C-BC/MB, the N/S-CNF shows a type I isotherm due to the accomplishment of the predominant adsorption of N_2 below the relative pressure (P/P_0) of 0.02, implying the presence of micro-pores. In addition, a hysteresis loop at P/P_0 from 0.40 to 1.0 is also observed, which is a characteristic of mesoporous materials. The pore size distribution (PSD) and surface area were calculated with the slit/cylinder model of quenched solid density functional theory using the adsorption branch. The PSD curve further confirms that both the micro-pore centering at 1.0 nm and the meso-pores with various sizes in 2–35 nm coexist in the N/S-CNF. The calculated surface area is $729 \text{ g}\cdot\text{cm}^{-2}$. The C-BC has similar PSD but smaller surface area, while the C-BC/MB belongs to the mesoporous material and has the smallest surface area. These results suggest that the MB or its decomposition product destroyed the micro-pores of C-BC, but the PMB promoted to form more micro-pores in the C-BC, probably by chemical etching the carbon matrix. The hierarchical porous structure and high surface area of N/S-CNF are beneficial to the exposure of more active sites and the diffusion of reactants.

To elucidate the crystallinity of N/S-CNF, X-ray powder diffraction (XRD) and Raman spectroscopic investigation were conducted. The XRD patterns of the N/S-CNF and the control samples show a broad peak at approximately $2\theta = 24^\circ$ and a very weak peak at $2\theta = 42^\circ$ (Figure 5b), which are the characteristics of graphitic carbon materials with low graphitization degree [40]. Raman spectra (Figure 5c) further reveal that both amorphous and crystalline carbon coexist in these samples. The intensity ratios of the D to G bands (I_D/I_G) are nearly same for these samples, reflecting their similar graphitization degree [41].

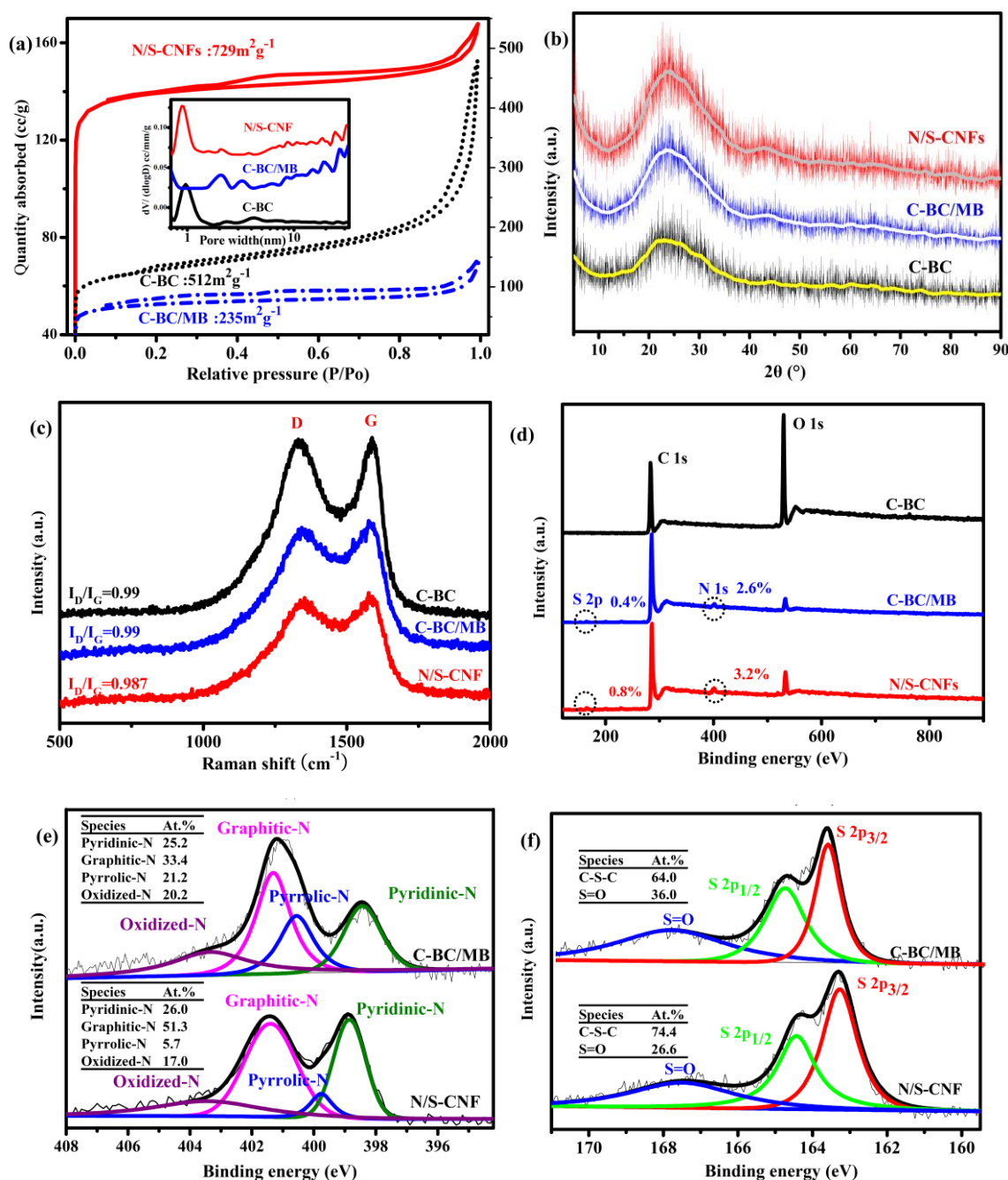


Figure 5. (a) N_2 adsorption-desorption isotherms and the inset is the pore size distribution curve; (b) XRD patterns; (c) Raman spectra and (d) XPS full spectra of C-BC, C-BC/MB and N/S-CNF; (e) $N1s$ and (f) $S2p$ fine XPS spectra of C-BC/MB and N/S-CNF.

To further confirm the chemical state of N and S, X-ray photo electron spectroscopy (XPS) measurement was carried out. As shown the XPS survey spectra in Figure 5d, N and S are detected from the N/S-CNF and C-BC/MB, confirming that the N and S atoms have been successfully introduced into the carbon matrix, which is in agreement with the EDS results. However, the contents of N and S in the N/S-CNF are 3.2% and 0.8%, respectively, which are higher than that (2.6% and 0.4%) of the C-BC/MB. Generally, It is believed that the N and S content play a key role for the improved ORR catalytic activity [13,42], and thus the N/S-CNF should have better catalysis performance than that of C-BC/MB. In addition, it is reported that the N and S species proportion also is crucial for the

ORR catalytic activity of electrocatalyst [43]. From the high-resolution N1s spectra (Figure 5e) of the N/S-CNF and C-BC/MB, four peaks can be deconvoluted into, which are assigned to the pyridinic N (398.7 eV), pyrrolic N (399.8 eV), graphitic N (401.2 eV) and (403.2eV), respectively. Usually, it is accepted that the pyridinic N and graphitic N are active species for the ORR [43]. Compared with the C-BC/MP, the N/S-CNF has a higher amount (77.3 at. %) of the two species and thus should display better catalysis performance for the ORR. In addition, the high-resolution S2p spectra (Figure 5f) show the peaks of $P_{1/2}$ and $P_{3/2}$ at binding energy of 163.5 and 164.3 eV which attribute to C–S–C bonds, and the ones at 166.0–170 eV are associated with the oxidized-S species that are chemically inactive for the ORR [30]. Similar to the case of N, the N/S-CNF also possesses higher amount (74.4%) of the active S species than that (64%) of C-BC/MP. Therefore, combining all the above results of SEM, PSD, XRD, XPS, and so on, a conclusion can be drawn that the PMB is more suitable as N and S source to prepare efficient electrocatalyst for the ORR than the MB.

2.3. Electrocatalytic Activity of the N/S-CNF for the ORR

The electrocatalytic activity of the N/S-CNF for the ORR was evaluated by cyclic voltammetry (CV) measurements in 0.1 M KOH electrolyte. Being compared with the smooth CV curve obtained from the N_2 -saturated electrolyte (Figure 6a), the CV curve in O_2 -saturated electrolyte shows a cathodic peak at 0.78 V, implying the electrocatalytic activity of N/S-CNF for the ORR in alkaline media. The ORR performance of the N/S-CNF was further measured with the rotating disk electrode (RDE) using linear sweep voltammetry (LSV) technique. As control subjects, the ORR activities of the C-BC, C-BC/MB and Pt/C electrocatalyst were also tested under the same experimental conditions (Figure 6b). Unsurprisingly, the C-BC shows the worst catalytic activity due to lacking active centres derived from N/S doping. With the benefit of N/S doping, the C-BC/MB exhibits a significant performance boost over the C-BC. Especially, with the aid of the large surface area and high amount of active N and S species, the N/S-CNF shows the best catalytic performance for the ORR, featuring with a comparable $E_{1/2}$ value (0.80 V) to the commercial 20 wt % Pt/C (0.83 V). In addition, the $E_{1/2}$ value (0.80 V) is also more positive than some of the reported N,S-co-doped carbon-based electrocatalysts (Table 1). Especially, the $E_{1/2}$ (0.80 V) in this work is 170 mV higher than that reported N-S-CNF-800 (MB) [31], which was prepared through BC physically absorbing MB and followed the carbonization process. We think the novel preparation method should be responsible for the improved catalytic activity. Firstly, based on the adsorption kinetic of MB on the cellulose [44] a harsh adsorption condition, heating the saturated solution of MB containing the dried BC at 100 °C for 4.5 h with autoclave, was employed to increase the adsorption amount of MB. Secondly, the N/S-CNF was obtained by carbonizing the BC/PMB hybrid that derived from the in situ polymerization of MB on the BC surface, but not by directly carbonizing the BC/MB hybrid as mentioned in the literature [31]. Obviously, compared with the small molecule compound, N,S-containing polymer is much more suitable as N/S source for the synthesis of carbon-based electrocatalyst with high ORR catalytic activity. To clarify the influence of synthesis parameters on the catalytic activity of N/S-CNF, a series of samples were prepared. The corresponding LSV curves for the ORR (Figure S5) reveal that the catalytic activity of N/S-CNF is sensitive to the synthesis condition, and the optimized experimental parameters are critical for achieving the N/S-CNF with high catalytic activity.

The catalysis kinetic of the N/S-CNF for the ORR was further investigated. It is normal that the limiting diffusion current increases with the rotation speed due to the thinned diffusion layer (Figure 6c). The transferred electron number (n) per oxygen molecule involved in the ORR process was calculated with Koutecky–Levich equation, which was to be ca. 3.89 in the potential range of 0.4 to 0.6 V, demonstrating an approximate four-electron pathway. To elucidate the electron transfer mechanism, the hydrogen peroxide yields were measured with rotating ring-disk electrode (RRDE). As shown in Figure 6f, the ring current originating from the oxidation of hydrogen peroxide ions (HO_2^-) is low. The calculated percentage of HO_2^- is below 17% over the potential range from 0.2 to 0.8 V, which corresponds to a transfer number of ~ 3.88 . This is agreement with the results obtained

from the Koutecky–Levich plots, again illuminating a nearly $4e^-$ pathway for the ORR catalyzed by the N/S-CNF.

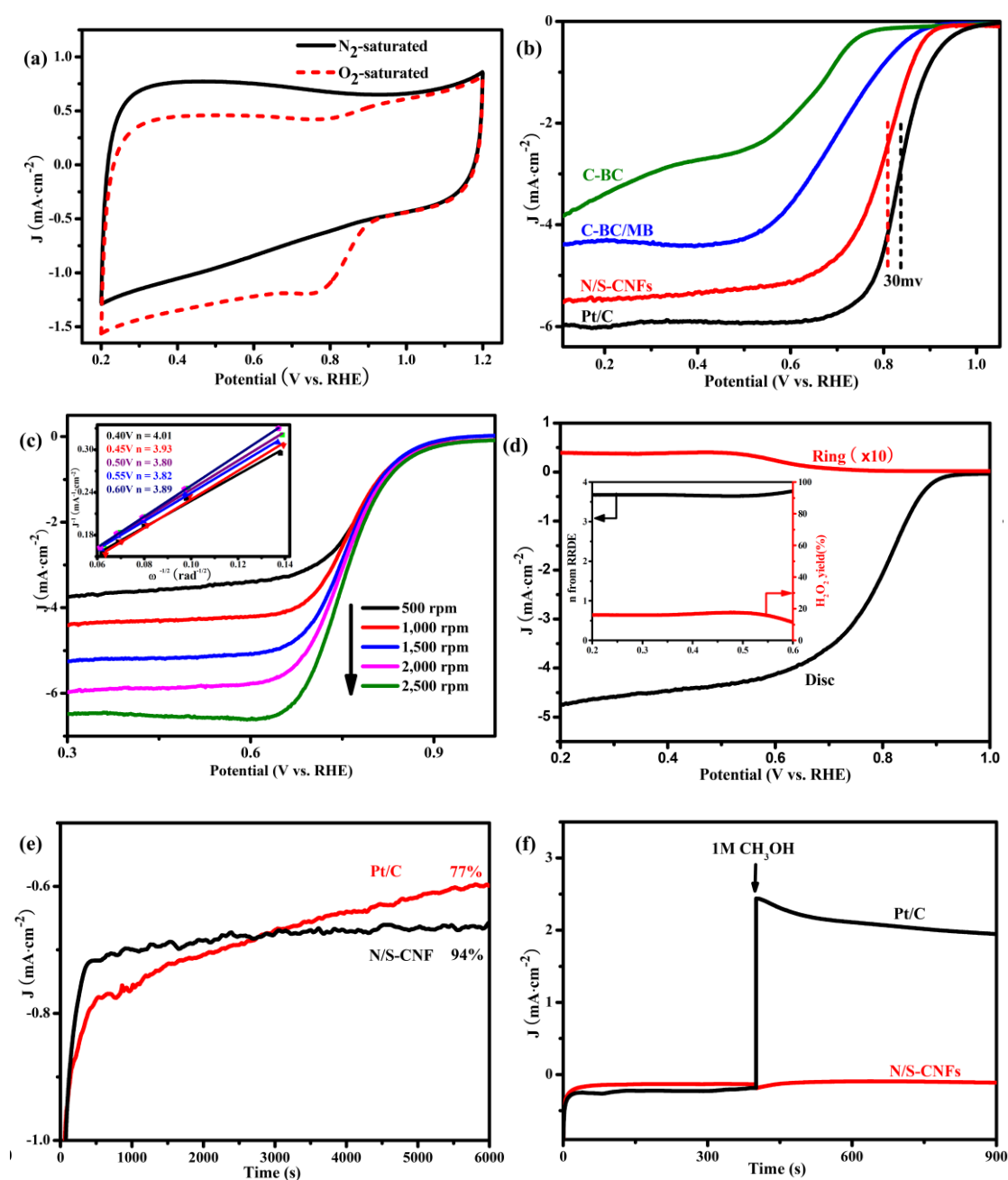


Figure 6. (a) CV curves of the N/S-CNF in N_2/O_2 -saturated 0.1 M KOH solution at scan rate of $50 \text{ mV} \cdot \text{s}^{-1}$; (b) ORR polarization curves of the C-BC, C-BC/MB, N/S-CNF and Pt/C electrocatalysts at scan rate of $10 \text{ mV} \cdot \text{s}^{-1}$ and a rotation rate of 1600 rpm; (c) LSV curves of N/S-CNF at different rotation rates, and the inset is the corresponding Koutecky–Levich plots; (d) RRDE measurements for N/S-CNF electrode; chronoamperometry curves of the N/S-CNF and Pt/C obtained at 0.75 V for (e) the stability test; and (f) methanol tolerance test before and after adding 1 M methanol. (b–f) were obtained in O_2 -saturated 1 M KOH solution.

Table 1. The difference of half wave potential between the N/S-co-doped carbon-based electrocatalyst and 20 wt % Pt/C for the ORR in 0.1 M KOH solution.

Sample	$\Delta E_{\frac{1}{2}}$ (mV)	Ref.
N/S-CNFs	30	This work
N-S-CNF-800 (MB)	200	[31]
NS-3DrGO-950	64	[43]
N,S-PGN-800	30	[45]
NSC800	35.4	[46]
NSC-A2	80	[47]
PAC-5S	48	[48]
S1N5-OMC	65	[49]
N/S-2DPC-60	27	[50]
N,S-hcs-900 °C	40	[51]
NS-G	72	[52]
N,S-CN	50	[53]
CNx/CSx-GNRs 1000° for 2.5 h	50	[54]

Subsequently, the chronoamperometric responses is used to evaluate the electrocatalytic activity and stability of the N/S-CNF. As shown in Figure 6e, after a brief transient period, the oxygen reduction current at the N/S-CNF electrode remains stable for the long time (6000 s) of polarization, while the current at the Pt/C electrode reduced to about 77% during the same test period, implying the excellent durability of the N/S-CNF.

Methanol-tolerance is an important benchmark for the electrocatalyst used in fuel cells, the catalysis performance of the N/S-CNF in KOH electrolyte containing methanol was investigated by chronoamperometry. As displayed in Figure 6f, after adjusting the concentration of methanol to 1 M in the O₂-saturated 0.1 M KOH electrolyte, the ORR current for Pt/C electrocatalyst shows a drastic surge and cannot be recovered to the initial level. Conversely, the current level of the N/S-CNF remains virtually unchanged, indicating its excellent methanol-tolerance.

3. Materials and Methods

3.1. Materials

BC membranes were supplied by Hainan Yida Food Co., Ltd., (Hainan, China), stored in acetic acid solution. Before use, BC membranes were immersed into a 0.1 M sodium hydroxide solution at 100 °C for 60 min to remove the residual cells, and then thoroughly washed with deionized water until pH reached neutral. To facilitate experimental operation, the BC membranes were cut to quadrate pieces with size of 3 × 3 cm, and followed by freeze drying at −50 °C. All other chemicals were purchased from Aladdin Reagent Co. Ltd., (Shanghai, China) and used as received.

3.2. Preparation of BC/MB and BC/PMB

6 mL of the saturated solution of MB was poured into the autoclave with volume of 15 mL, and the dried BC membranes of 15 mg were soaked into it. To accelate adsorption of MB on BC membrane, the autoclave was sealed and heated at 100 °C for 4.5 h. The blued BC membranes were washed by water to remove the physically adsorbed day molecules, and then immersed into 10 mL of ammonium peroxydisulphate solution (0.1 M) for 1.5 h to make the methylene blue polymerize. The purple BC membranes were freeze-dried, and transferred into a tubular furnace for carbonization under a flowing N₂ atmosphere at 800 °C for 2 h with a heating rate of 2 °C·min^{−1}. After cooled to room temperature, the black carbon powder coded as N/S-CNF was achieved. To compare, the controlled samples were also prepared with the BC membranes adsorbing and unadsorbing MB by the similar process.

3.3. Electrochemical Measurements

Electrochemical experiments were carried out by computer-controlled CHI 760E (Chenhua Instrument, Shanghai, China) electrochemical workstation equipped with RDE apparatus at room temperature, using a standard three-electrode system. The electrocatalyst-modified working electrode was prepared with the electrocatalyst ink, which was obtained by mixing 10 mg of electrocatalyst and 5 mL of water/Nafion solution, and sonicating the mixture for 60 min. After the working electrode loaded 10 μ L of electrocatalyst ink was dried at room temperature, the CV and LSV tests were measured in N_2 - or O_2 -saturated 0.1 M KOH solution, by using a saturated calomel and carbon rod as reference electrode and counter electrode, respectively. All potentials in this work were reported with respect to reversible hydrogen electrode (RHE). The electron transfer number (n) was determined by the Koutecky–Levich equation:

$$1/j = 1/j_k + 1/B\omega^{0.5} \quad (1)$$

Here, j_k is the kinetic current density, and B is expressed by the following expression:

$$B = 0.2 \times n \times F \times (D_{O_2})^{2/3} \times \nu^{-1/6} \times C_{O_2} \quad (2)$$

where n represents the number of electrons transferred per oxygen molecule; F is the Faraday constant ($F = 96,485 \text{ C} \cdot \text{mol}^{-1}$); D_{O_2} is the diffusion coefficient of O_2 in 0.1 M KOH ($1.9 \times 10^{-5} \text{ cm}^2 \cdot \text{s}^{-1}$); ν is the kinematic viscosity of the electrolyte solution ($0.01 \text{ cm}^2 \cdot \text{s}^{-1}$); C_{O_2} is the concentration of dissolved O_2 ($1.2 \times 10^{-6} \text{ mol} \cdot \text{cm}^{-3}$). The constant 0.2 is adopted when the rotation speed is expressed in rpm.

The n and H_2O_2 yield (%) were measured with RRDE, and calculated with the followed equations:

$$n = 4I_d / (I_d + I_r/N) \quad (3)$$

$$H_2O_2 (\%) = 100 \times (4 - n)/2 \quad (4)$$

where I_d is the disk current density, I_r is the ring current density, and $N = 0.37$ is the current collection efficiency.

3.4. Characterization

The crystalline structure, morphology and surface composition of sample were physically characterized by XRD (D/max-rC) (Rigaku, Tokyo, Japan), TEM (JEM-2100F) (JEOL, Tokyo, Japan) equipped with EDS, SEM (SU-8020) (Hitachi High-Technologies Corp., Japan), Raman Spectrometer (In Via Reflex) (Renishaw PLC, Wotton-under-Edge, UK) and XPS (AXIS ULTRA) (Kratos Analytical Ltd., Hadano, Japan). The surface area and pore volume of the samples were measured on a physical adsorption instrument (ASAP 2400) (Norcross, GA, USA), the functional groups were analyzed by using Fourier transform infrared spectroscopy (FTIR, Nicolet Is10) (Thermo Fisher Scientific, Waltham, MA, USA), and the thermal decomposition behavior was measured by TGA (Q600) (TA Instruments, New Castle, DE, USA).

4. Conclusions

We developed a facile method to fabricate superior ORR catalysts. By simply in situ polymerization of MB on the surface of BC, followed by carbonization, the N/S-CNF nanomaterials was obtained. It was found that, compared with the small molecular substance, the polymer as nitrogen/sulfur source can significantly enhance the catalytic activity of the resultant N,S-co-doped carbon nanofibers. Benefited from the synergistic effect of the multiple active sites, as well as the enriched porosity and high surface area, the N/S-CNF revealed excellent ORR activity in alkaline media with a half-wave potential of about 0.80 V. Moreover, the N/S-CNF showed better long-term stability and methanol tolerance than that commercial 20 wt % Pt/C, demonstrating its potential application in fuel cells and metal-air batteries as alternative Pt electrocatalysts.

Supplementary Materials: The following are available online at <http://www.mdpi.com/2073-4344/8/7/269/s1>, Figure S1: EDS spectra of (a) the BC/MB and (b) BC/PMB, Figure S2: SEM image of the PMB, Figure S3: The dark field TEM image of the C-BC/MB and the corresponding element mapping images of S, N, O and C, Figure S4: The diameter (b) and length (c) distribution of the nanofibers obtained from TEM image (a) of the sample N/S-CNF, Figure S5: Linear sweep voltammetry curves of the samples of N/S-CNF prepared at different condition. Fixed the other experiment parameters, (a) the concentration of MB in the adsorption process of MB on BC was varied from 0.01 to 0.1 mol/L; (b) the heat treatment temperature in the adsorption process of MB on BC was varied from 60 to 150 °C; (c) the polymerization time of MB was varied from 0.5 to 6 h. All these linear sweep voltammetry curves were obtained from O₂-saturated 0.1 M KOH solution at scan rate of 10 mv/s and a rotation rate of 1600 rpm.

Author Contributions: J.L. analyzed and interpreted the experiment data; Y.-G.J., B.Q., F.Z. and H.G. performed the experiments and collected data; P.C. designed the experiments and drafted the article; Y.C., and Z.A. critically revised the article; X.C. given final approval of the version to be published.

Acknowledgments: This research was supported by National Science Foundation Committee of China (51773112), Program for Science & Technology Innovation Team of Shaanxi Province (2018TD-030), the Fundamental Research Funds for the Central Universities (GK201801001, GK201703030).

Conflicts of Interest: The authors declare no conflict of interest.

References

1. Fu, J.; Cano, Z.P.; Park, M.G.; Yu, A.; Fowler, M.; Chen, Z. Electrically rechargeable zinc-air batteries: Progress, challenges, and perspectives. *Adv. Mater.* **2017**, *29*, 1604685. [[CrossRef](#)] [[PubMed](#)]
2. Tang, C.; Zhang, Q. Nanocarbon for oxygen reduction electrocatalysis: Dopants, edges, and defects. *Adv. Mater.* **2017**, *29*, 1604103. [[CrossRef](#)] [[PubMed](#)]
3. Shao, M.; Chang, Q.; Dodelet, J.-P.; Chenitz, R. Recent advances in electrocatalysts for oxygen reduction reaction. *Chem. Rev.* **2016**, *116*, 3594–3657. [[CrossRef](#)] [[PubMed](#)]
4. Pan, J.; Xu, Y.Y.; Yang, H.; Dong, Z.; Liu, H.; Xia, B.Y. Advanced architectures and relatives of air electrodes in Zn-air batteries. *Adv. Sci.* **2018**, *5*, 1700691:1–1700691:30. [[CrossRef](#)] [[PubMed](#)]
5. Xu, H.; Yan, B.; Li, S.; Wang, J.; Wang, C.; Guo, J.; Du, Y. Facile construction of N-doped graphene supported hollow ptag nanodendrites as highly efficient electrocatalysts toward formic acid oxidation reaction. *ACS Sustain. Chem. Eng.* **2018**, *6*, 609–617. [[CrossRef](#)]
6. Cheng, H.; Li, M.L.; Su, C.Y.; Li, N.; Liu, Z.Q. Cu-Co bimetallic oxide quantum dot decorated nitrogen-doped carbon nanotubes: A high-efficiency bifunctional oxygen electrode for Zn-air batteries. *Adv. Funct. Mater.* **2017**, *27*, 1701833. [[CrossRef](#)]
7. Liu, X.; Amiin Ibrahim, S.; Liu, S.; Pu, Z.; Li, W.; Ye, B.; Tan, D.; Mu, S. H₂O₂-assisted synthesis of porous N-doped graphene/molybdenum nitride composites with boosted oxygen reduction reaction. *Adv. Mater. Interfaces* **2017**, *4*, 1601227. [[CrossRef](#)]
8. Su, C.Y.; Cheng, H.; Li, W.; Liu, Z.Q.; Li, N.; Hou, Z.; Bai, F.Q.; Zhang, H.X.; Ma, T.Y. Atomic modulation of FeCo-nitrogen-carbon bifunctional oxygen electrodes for rechargeable and flexible all-solid-state zinc-air battery. *Adv. Energy Mater.* **2017**, *7*, 1602420. [[CrossRef](#)]
9. Cui, H.; Zhou, Z.; Jia, D. Heteroatom-doped graphene as electrocatalysts for air cathodes. *Mater. Horiz.* **2017**, *4*, 7–19. [[CrossRef](#)]
10. Zhu, C.; Li, H.; Fu, S.; Du, D.; Lin, Y. Highly efficient nonprecious metal catalysts towards oxygen reduction reaction based on three-dimensional porous carbon nanostructures. *Chem. Soc. Rev.* **2016**, *45*, 517–531. [[CrossRef](#)] [[PubMed](#)]
11. Lee Won, J.; Lim, J.; Kim Sang, O. Nitrogen dopants in carbon nanomaterials: Defects or a new opportunity? *Small Methods* **2016**, *1*, 1600014.
12. Xiang, Z.; Cao, D.; Huang, L.; Shui, J.; Wang, M.; Dai, L. Nitrogen-doped holey graphitic carbon from 2D covalent organic polymers for oxygen reduction. *Adv. Mater.* **2014**, *26*, 3315–3320. [[CrossRef](#)] [[PubMed](#)]
13. Yu, H.; Shang, L.; Bian, T.; Shi, R.; Waterhouse Geoffrey, I.N.; Zhao, Y.; Zhou, C.; Wu, L.Z.; Tung, C.H.; Zhang, T. Nitrogen-doped porous carbon nanosheets templated from g-C₃N₄ as metal-free electrocatalysts for efficient oxygen reduction reaction. *Adv. Mater.* **2016**, *28*, 5080–5086. [[CrossRef](#)] [[PubMed](#)]
14. Chatterjee, K.; Ashokkumar, M.; Gullapalli, H.; Gong, Y.; Vajtai, R.; Thanikaivelan, P.; Ajayan, P.M. Nitrogen-rich carbon nano-onions for oxygen reduction reaction. *Carbon* **2018**, *130*, 645–651. [[CrossRef](#)]

15. Geng, D.; Chen, Y.; Chen, Y.; Li, Y.; Li, R.; Sun, X.; Ye, S.; Knights, S. High oxygen-reduction activity and durability of nitrogen-doped graphene. *Energy Environ. Sci.* **2011**, *4*, 760–764. [[CrossRef](#)]
16. Li, L.; Dai, P.; Gu, X.; Wang, Y.; Yan, L.; Zhao, X. High oxygen reduction activity on a metal-organic framework derived carbon combined with high degree of graphitization and pyridinic-N dopants. *J. Mater. Chem. A* **2017**, *5*, 789–795. [[CrossRef](#)]
17. Zhao, J.; Liu, Y.; Quan, X.; Chen, S.; Yu, H.; Zhao, H. Nitrogen-doped carbon with a high degree of graphitization derived from biomass as high-performance electrocatalyst for oxygen reduction reaction. *Appl. Surf. Sci.* **2017**, *396*, 986–993. [[CrossRef](#)]
18. Zhan, Y.; Yu, X.; Cao, L.; Zhang, B.; Wu, X.; Xie, F.; Zhang, W.; Chen, J.; Xie, W.; Mai, W.; et al. The influence of nitrogen source and doping sequence on the electrocatalytic activity for oxygen reduction reaction of nitrogen doped carbon materials. *Int. J. Hydrogen Energy* **2016**, *41*, 13493–13503. [[CrossRef](#)]
19. Higgins, D.; Chen, Z.; Chen, Z. Nitrogen doped carbon nanotubes synthesized from aliphatic diamines for oxygen reduction reaction. *Electrochim. Acta* **2011**, *56*, 1570–1575. [[CrossRef](#)]
20. Lin, C.Y.; Zhang, D.; Zhao, Z.; Xia, Z. Covalent organic framework electrocatalysts for clean energy conversion. *Adv. Mater.* **2017**, *30*, 1703646. [[CrossRef](#)] [[PubMed](#)]
21. Xu, Q.; Tang, Y.; Zhang, X.; Oshima, Y.; Chen, Q.; Jiang, D. Template conversion of covalent organic frameworks into 2d conducting nanocarbons for catalyzing oxygen reduction reaction. *Adv. Mater.* **2018**, *30*, 1706330. [[CrossRef](#)] [[PubMed](#)]
22. Zhou, H.; Zhang, J.; Amiin, I.S.; Zhang, C.; Liu, X.; Tu, W.; Pan, M.; Mu, S. Transforming waste biomass with an intrinsically porous network structure into porous nitrogen-doped graphene for highly efficient oxygen reduction. *Phys. Chem. Chem. Phys.* **2016**, *18*, 10392–10399. [[CrossRef](#)] [[PubMed](#)]
23. Gao, S.; Li, X.; Li, L.; Wei, X. A versatile biomass derived carbon material for oxygen reduction reaction, supercapacitors and oil/water separation. *Nano Energy* **2017**, *33*, 334–342. [[CrossRef](#)]
24. Zheng, X.; Cao, X.; Li, X.; Tian, J.; Jin, C.; Yang, R. Biomass lysine-derived nitrogen-doped carbon hollow cubes via a nacl crystal template: An efficient bifunctional electrocatalyst for oxygen reduction and evolution reactions. *Nanoscale* **2017**, *9*, 1059–1067. [[CrossRef](#)] [[PubMed](#)]
25. Lin, G.; Ma, R.; Zhou, Y.; Liu, Q.; Dong, X.; Wang, J. Koh activation of biomass-derived nitrogen-doped carbons for supercapacitor and electrocatalytic oxygen reduction. *Electrochim. Acta* **2018**, *261*, 49–57. [[CrossRef](#)]
26. Chen, W.; Yu, H.; Lee, S.-Y.; Wei, T.; Li, J.; Fan, Z. Nanocellulose: A promising nanomaterial for advanced electrochemical energy storage. *Chem. Soc. Rev.* **2018**, *47*, 2837–2872. [[CrossRef](#)] [[PubMed](#)]
27. Wu, Z.-Y.; Liang, H.-W.; Chen, L.-F.; Hu, B.-C.; Yu, S.-H. Bacterial cellulose: A robust platform for design of three dimensional carbon-based functional nanomaterials. *Acc. Chem. Res.* **2016**, *49*, 96–105. [[CrossRef](#)] [[PubMed](#)]
28. Liang, H.-W.; Wu, Z.-Y.; Chen, L.-F.; Li, C.; Yu, S.-H. Bacterial cellulose derived nitrogen-doped carbon nanofiber aerogel: An efficient metal-free oxygen reduction electrocatalyst for zinc-air battery. *Nano Energy* **2015**, *11*, 366–376. [[CrossRef](#)]
29. Pei, Z.; Li, H.; Huang, Y.; Xue, Q.; Huang, Y.; Zhu, M.; Wang, Z.; Zhi, C. Texturing in situ: N,S-enriched hierarchically porous carbon as a highly active reversible oxygen electrocatalyst. *Energy Environ. Sci.* **2017**, *10*, 742–749. [[CrossRef](#)]
30. Rafatullah, M.; Sulaiman, O.; Hashim, R.; Ahmad, A. Adsorption of methylene blue on low-cost adsorbents: A review. *J. Hazard. Mater.* **2010**, *177*, 70–80. [[CrossRef](#)] [[PubMed](#)]
31. Wu, Z.-Y.; Liang, H.-W.; Li, C.; Hu, B.-C.; Xu, X.-X.; Wang, Q.; Chen, J.-F.; Yu, S.-H. Dyeing bacterial cellulose pellicles for energetic heteroatom doped carbon nanofiber aerogels. *Nano Res.* **2014**, *7*, 1861–1872. [[CrossRef](#)]
32. Guo, D.; Shibuya, R.; Akiba, C.; Saji, S.; Kondo, T.; Nakamura, J. Active sites of nitrogen-doped carbon materials for oxygen reduction reaction clarified using model catalysts. *Science* **2016**, *351*, 361–365. [[CrossRef](#)] [[PubMed](#)]
33. Tang, Z.; Wang, L.; Ma, Z. Triple sensitivity amplification for ultrasensitive electrochemical detection of prostate specific antigen. *Biosens. Bioelectron.* **2017**, *92*, 577–582. [[CrossRef](#)] [[PubMed](#)]
34. Lv, X.; Zhang, P.; Li, M.; Guo, Z.; Zheng, X. Synthesis of polymethylene blue nanoparticles and their application to label-free DNA detection. *Anal. Lett.* **2016**, *49*, 2728–2740. [[CrossRef](#)]
35. Li, X.; Zhong, M.; Sun, C.; Luo, Y. A novel bilayer film material composed of polyaniline and poly(methylene blue). *Mater. Lett.* **2005**, *59*, 3913–3916. [[CrossRef](#)]

36. Shan, J.; Wang, L.; Ma, Z. Novel metal-organic nanocomposites: Poly(methylene blue)-Au and its application for an ultrasensitive electrochemical immunosensing platform. *Sensor. Actuators B Chem.* **2016**, *237*, 666–671. [[CrossRef](#)]
37. Xiao, X.; Zhou, B.; Tan, L.; Tang, H.; Zhang, Y.; Xie, Q.; Yao, S. Poly(methylene blue) doped silica nanocomposites with crosslinked cage structure: Electropolymerization, characterization and catalytic activity for reduction of dissolved oxygen. *Electrochim. Acta* **2011**, *56*, 10055–10063. [[CrossRef](#)]
38. Yang, S.; Li, G.; Zhao, J.; Zhu, H.; Qu, L. Electrochemical preparation of ag nanoparticles/poly(methylene blue) functionalized graphene nanocomposite film modified electrode for sensitive determination of rutin. *J. Electroanal. Chem.* **2014**, *717–718*, 225–230. [[CrossRef](#)]
39. Rincón Rosalba, A.; Artyushkova, K.; Mojica, M.; Germain Marguerite, N.; Minter Shelley, D.; Atanassov, P. Structure and electrochemical properties of electrocatalysts for nadh oxidation. *Electroanalysis* **2010**, *22*, 799–806. [[CrossRef](#)]
40. Zheng, F.; Yang, Y.; Chen, Q. High lithium anodic performance of highly nitrogen-doped porous carbon prepared from a metal-organic framework. *Nat. Commun.* **2014**, *5*, 5261. [[CrossRef](#)] [[PubMed](#)]
41. Chen, L.-F.; Lu, Y.; Yu, L.; Lou, X.W. Designed formation of hollow particle-based nitrogen-doped carbon nanofibers for high-performance supercapacitors. *Energy Environ. Sci.* **2017**, *10*, 1777–1783. [[CrossRef](#)]
42. Klingele, M.; Pham, C.; Vuyyuru, K.R.; Britton, B.; Holdcroft, S.; Fischer, A.; Thiele, S. Sulfur doped reduced graphene oxide as metal-free catalyst for the oxygen reduction reaction in anion and proton exchange fuel cells. *Electrochem. Commun.* **2017**, *77*, 71–75. [[CrossRef](#)]
43. Li, Y.; Yang, J.; Huang, J.; Zhou, Y.; Xu, K.; Zhao, N.; Cheng, X. Soft template-assisted method for synthesis of nitrogen and sulfur co-doped three-dimensional reduced graphene oxide as an efficient metal free catalyst for oxygen reduction reaction. *Carbon* **2017**, *122*, 237–246. [[CrossRef](#)]
44. Chan, C.H.; Chia, C.H.; Zakaria, S.; Sajab, M.S.; Chin, S.X. Cellulose nanofibrils: a rapid adsorbent for the removal of methylene blue. *RSC Adv.* **2015**, *5*, 18204–18212. [[CrossRef](#)]
45. Wu, M.; Liu, Y.; Zhu, Y.; Lin, J.; Liu, J.; Hu, H.; Wang, Y.; Zhao, Q.; Lv, R.; Qiu, J. Supramolecular polymerization-assisted synthesis of nitrogen and sulfur dual-doped porous graphene networks from petroleum coke as efficient metal-free electrocatalysts for the oxygen reduction reaction. *J. Mater. Chem. A* **2017**, *5*, 11331–11339. [[CrossRef](#)]
46. Xu, L.; Fan, H.; Huang, L.; Xia, J.; Li, S.; Li, M.; Ding, H.; Huang, K. Chrysanthemum-derived n and s co-doped porous carbon for efficient oxygen reduction reaction and aluminum-air battery. *Electrochim. Acta* **2017**, *239*, 1–9. [[CrossRef](#)]
47. Yang, S.; Mao, X.; Cao, Z.; Yin, Y.; Wang, Z.; Shi, M.; Dong, H. Onion-derived n, s self-doped carbon materials as highly efficient metal-free electrocatalysts for the oxygen reduction reaction. *Appl. Surf. Sci.* **2018**, *427*, 626–634. [[CrossRef](#)]
48. You, C.; Jiang, X.; Han, L.; Wang, X.; Lin, Q.; Hua, Y.; Wang, C.; Liu, X.; Liao, S. Uniform nitrogen and sulphur co-doped hollow carbon nanospheres as efficient metal-free electrocatalysts for oxygen reduction. *J. Mater. Chem. A* **2017**, *5*, 1742–1748. [[CrossRef](#)]
49. Jiang, T.; Wang, Y.; Wang, K.; Liang, Y.; Wu, D.; Tsiakaras, P.; Song, S. A novel sulfur-nitrogen dual doped ordered mesoporous carbon electrocatalyst for efficient oxygen reduction reaction. *Appl. Catal. B Environ.* **2016**, *189*, 1–11. [[CrossRef](#)]
50. Su, Y.; Yao, Z.; Zhang, F.; Wang, H.; Mics, Z.; Cánovas, E.; Bonn, M.; Zhuang, X.; Feng, X. Sulfur-enriched conjugated polymer nanosheet derived sulfur and nitrogen co-doped porous carbon nanosheets as electrocatalysts for oxygen reduction reaction and zinc-air battery. *Adv. Funct. Mater.* **2016**, *26*, 5893–5902. [[CrossRef](#)]
51. Wu, Z.; Liu, R.; Wang, J.; Zhu, J.; Xiao, W.; Xuan, C.; Lei, W.; Wang, D. Nitrogen and sulfur co-doping of 3D hollow-structured carbon spheres as an efficient and stable metal free catalyst for the oxygen reduction reaction. *Nanoscale* **2016**, *8*, 19086–19092. [[CrossRef](#)] [[PubMed](#)]
52. Pan, F.; Duan, Y.; Zhang, X.; Zhang, J. A facile synthesis of nitrogen/sulfur co-doped graphene for the oxygen reduction reaction. *ChemCatChem* **2015**, *8*, 163–170. [[CrossRef](#)]

53. Qu, K.; Zheng, Y.; Dai, S.; Qiao, S.Z. Graphene oxide-polydopamine derived n, s-codoped carbon nanosheets as superior bifunctional electrocatalysts for oxygen reduction and evolution. *Nano Energy* **2016**, *19*, 373–381. [[CrossRef](#)]
54. Zehtab Yazdi, A.; Roberts, E.P.L.; Sundararaj, U. Nitrogen/sulfur co-doped helical graphene nanoribbons for efficient oxygen reduction in alkaline and acidic electrolytes. *Carbon* **2016**, *100*, 99–108. [[CrossRef](#)]



© 2018 by the authors. Licensee MDPI, Basel, Switzerland. This article is an open access article distributed under the terms and conditions of the Creative Commons Attribution (CC BY) license (<http://creativecommons.org/licenses/by/4.0/>).